

# Hypervelocity Impact of Unstressed and Stressed Titanium in a Whipple Configuration in Support of the Orion Crew Exploration Vehicle Service Module Propellant Tanks

Henry K. Nahra<sup>a1</sup>, Eric Christiansen<sup>b</sup>, Andrew Piekutowski<sup>c</sup>, Frankel Lyons<sup>b</sup>,  
Christopher Keddy<sup>d</sup>, Jonathan Salem<sup>a</sup>, Kevin Poormon<sup>c</sup>, William Bohl<sup>e</sup>, Joshua Miller<sup>e</sup>,  
Nathanael Greene<sup>d</sup>, Karen Rodriguez<sup>d</sup>

<sup>a</sup>NASA Glenn Research Center, 21000 Brookpark Rd., Cleveland, OH 44135

<sup>b</sup>NASA Johnson Space Center, 2101 NASA Parkway, Mail Code SX2, Houston, TX 77058

<sup>c</sup>University of Dayton Research Institute, 300 College Park Avenue, Dayton, OH 45469-0116

<sup>d</sup>White Sands Test Facility, P.O. Box 20, Las Cruces, NM 88004-0020

<sup>e</sup>Lockheed Martin Space Systems Co., P.O. Box 179, Denver, CO 80201

Received Date Line (to be inserted by Production) (8 pt)

---

## Abstract

Hypervelocity impacts were performed on six unstressed and six stressed titanium coupons with aluminium shielding in order to assess the effects of the partial penetration damage on the post impact micromechanical properties of titanium and on the residual strength after impact. This work is performed in support of the definition of the penetration criteria of the propellant and oxidizer tanks dome surfaces for the service module of the crew exploration vehicle where such a criterion is based on testing and analyses rather than on historical precedence. The objective of this work is to assess the effects of applied biaxial stress on the damage dynamics and morphology. The crater statistics revealed minute differences between stressed and unstressed coupon damage. The post impact residual stress analyses showed that the titanium strength properties were generally unchanged for the unstressed coupons when compared with undamaged titanium. However, high localized strains were shown near the craters during the tensile tests.

**Keywords:** Hypervelocity impacts, Titanium, projectiles, density, shielding, crater, residual strength, nylon projectile, Aluminum projectile

---

## 1. Introduction

The propellant tanks on the service module of the Orion crew exploration vehicle CEV are

---

<sup>1</sup> Corresponding Author, NASA-GRC, 21000 Brookpark Rd., Cleveland, OH 44135, (216) 433-5385 (office), 216 433-8050 (fax), [henry.k.nahra@nasa.gov](mailto:henry.k.nahra@nasa.gov)

vulnerable to the micrometeoroids and orbital debris (MMOD) impacts. Although they are shielded by other surfaces, a projectile of significant energy could penetrate through the shielding and fragmentation could impact the surfaces of the propellant and oxidizer tanks and result in adverse effects on the service module. The spectrum of damage ranges from a perforation through the tank wall to simple cratering of the surfaces of the tanks. The allowable depth of penetration in the surface of the propellant tank dome is integral to the definition of the failure criteria used in the MMOD system level analysis of the vehicle. The current allowable penetration criteria for the pressure vessels on board of the Service Module (SM) of the CEV are based on historical background; however, these criteria should be based on experiments and analyses that show that the allowable depth of penetration is reasonable and not overly conservative or non-conservative.

An experimental program aimed at addressing the depth of penetration that is allowed on the tanks surfaces with multi-center and multi-disciplinary participation was planned in support of NASA's future missions. Phase 1 of the program addresses the penetration depth of metallic titanium tank surfaces whereas phase 2 addresses the penetration depth into the composite surface of composite overwrapped (COPV) tanks. A building block approach is adopted in this program. For phase 1, which is concerned with the titanium surface, six stressed and unstressed titanium coupons shielded with aluminum shield were hypervelocity impacted by projectiles that penetrate the aluminum shield and cause the resulting plume to impact the titanium surface to produce a partial penetration distribution of craters. A series of post impact analyses are performed to assess the damage resulting from the craters. Detailed comparisons are performed to assess the difference between biaxially loaded and unstressed coupons impacted with similar projectiles and nearly similar velocities. Testing of pressurized titanium metal tanks is planned through task 2 of phase 1. This paper is focused on the hypervelocity impact (HVI) testing of the titanium coupons and the craters analyses that followed.

#### Nomenclature

C	Speed of sound in materials [km/s]
$d_p$	Projectile diameter [cm, mm]
E	Young's modulus [ksi, MPa]
H	Brinell hardness
HV	Vickers Hardness
$P_\infty$	Crater depth [cm]
$t_b$	Bumper thickness [cm]
$V_{\text{fragment}}$	Fragment velocity [km/s]
$V_p$	Projectile velocity [km/s]
$\epsilon_{xx}$	Strain along x direction [%]
$\epsilon_{yy}$	Strain along y direction [%]
$\sigma_{xx}$	Normal Stress Component along x direction [ksi, MPa]
$\sigma_{yy}$	Normal Stress Component along y direction [ksi, MPa]
$\nu$	Poisson Ratio
$\rho_p$	Projectile density [g/cm <sup>3</sup> ]
$\rho_t$	Target density [g/cm <sup>3</sup> ]

## 2. Testing

In this effort, the conducted HVI experiments consisted of performing six shots on aluminum-shielded unstressed titanium coupons at White Sands Test Facility (WSTF), and six shots on aluminum-shielded-biaxially-stressed titanium coupons at the University of Dayton Research Institute (UDRI)-Impact Physics Laboratories. The configurations of the test coupons were similar except for the biaxial stress state.

### 2.1 Target-Shielding Geometry

Figure 1 (a) shows a schematic of the coupon geometry. The basic configuration of the test article consisted of a 0.0965 cm (0.04") aluminium 6061-T6 bumper and a 0.127 cm (0.05") Titanium (Ti-6Al-4V) substrate with a standoff distance of 27.9 cm (11"). Similar configuration for the unstressed coupons was adopted. Although this geometry and configuration does not fully reflect the shielding design of the service module tanks, this configuration was chosen for the fact that it makes the crater analysis much more correlated with the projectile speed, density and velocity because the Whipple shield is well understood from a fundamental stand point. No material backing of the titanium was considered because we decided to pursue the worst case where the tank wall is contacting the gas and where the greatest mismatch in mechanical impedance occurs.

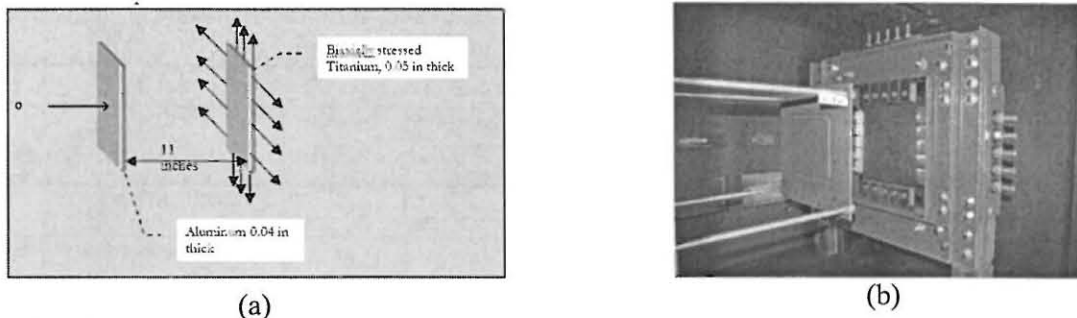


Fig. 1. (a) Shows a schematic of the experimental set up of the stressed Ti coupons and (b) shows the biaxial stress fixture with the titanium coupon installed

### 2.2 Biaxial Stress Fixture

A biaxial stress fixture was designed and fabricated at UDRI for this series of testing. It was based on the design of the uniaxial stress fixture used for the crack propagation studies of the International Space Station (ISS) module skin. The biaxial fixture is shown in Fig. 1(b). This fixture is capable of providing 80 ksi  $\pm$  7% of biaxial stress which was a requirement reflecting the stress state of typical metallic propellant tank. The calibration of the biaxial stress state was performed with eight biaxial strain gages (4 gauges in each direction). Five turnbuckles along the vertical and horizontal direction provided the mechanical pull to achieve the calibrated strain that corresponds to the desired stress level. The titanium coupons were first installed in the fixture. Before performing the hypervelocity impact, the titanium was strained to the appropriate strain level of 3248  $\mu$ strains in each direction based on the

aforementioned biaxial stress of 80 ksi. The strain level was computed from the two-dimensional Hooke's law given by,

$$\epsilon_{xx} = \frac{1}{E}(\sigma_{xx} - \nu\sigma_{yy}); \quad \epsilon_{yy} = \frac{1}{E}(\sigma_{yy} - \nu\sigma_{xx}) \quad (1)$$

Where  $\sigma_{xx}$  is the normal stress component along the x direction,  $\epsilon_{xx}$  is the strain along the x direction, E is Young's Modulus, and  $\nu$  is the Poisson ratio. The strain along the vertical direction is computed from the  $\epsilon_{yy}$  equation also given in Eqn. 1.

The titanium coupons for the unstressed tests were integrated with the aluminium shielding according to the spacing given in paragraph 2.1. For the stressed coupons, the configuration differed a little in that the titanium could not be integrated with the aluminium shielding. Instead, the aluminium shield was installed on a different structure as shown in Fig. 1(b) and titanium target was installed into the biaxial stress fixture. The titanium thickness was milled down to 0.127 cm (0.05") in an area in the middle of the coupon of 22.9×22.9 cm (9×9").

### 2.3 Test Matrices for the Unstressed and Stressed Coupons Tests.

The test plan matrix for the unstressed and stressed titanium coupons is shown in table 1 respectively. The first and second columns refer to the reference numbers of the tests performed at WSTF and UDRI respectively.

Table 1 –HVI tests on Unstressed and Stressed Ti coupons with Aluminum shields							
WSTF / HITF Number/	UDRI Test #	Seq.	Projectile Type	Projectile Diameter (mm)	Requested Velocity (km/s)	Impact Angle (deg)	Comments Ti thickness 1.27 mm (.05 in)
#1 HITF08373	#1	1	Al 2017-T4	1.6	7.0	0°	Estimated penetration of 0.165mm or 13%
#2 HITF08374	#2	2	Al 2017-T4	2.0	7.0	0°	Estimated penetration of 0.240mm or 19%
#3 HITF08375	#3	3	Al 2017-T4	2.6	7.0	0°	Estimated penetration of 0.370mm or 29%
#4 HITF08376	#4	4	Nylon	2.0	7.0	0°	Estimated penetration of 0.140mm or 11%
#5 HITF08377	#5	5	Nylon	3.6	7.0	0°	Estimated penetration of 0.340mm or 27%
#6 HITF08378	#6	6	Al 2017-T4	3.6	7.0	0°	Estimated penetration of 0.530mm or 42%

In general, the parameters were made very similar for comparison purposes in order to look for the effects of the biaxial stress on the micro-mechanical features of the craters and the residual strength of the titanium.

## 3. Results

The results for the unstressed and stressed titanium coupons HVIs will be presented in this section of the paper and these encompassed several post impact analyses performed on the craters.

### 3.1 Crater Depth Analyses.

Several craters in each of the impacted coupons were analyzed for depth and diameter. The craters were chosen based on their visual appearance as being of greater depth and diameter. The depth of penetration for each of the crater was measured with the 3D microscope at the Johnson Space Center. A typical depth image and profile is shown in Fig. 2. The craters were identified by placing and lining up a transparency over the titanium coupon and identifying with a marker the craters of interest. Then the transparency which served as a reference catalog was removed to look at the chosen craters. Table 2 shows the results of analyzing 5 craters on an unstressed titanium coupon where the projectile diameter was 1.6 mm at 6.69 km/s.

Figure 3 (a) and (b) shows the damage distribution on a stressed and unstressed titanium surface from a 2.6 mm projectile that impacted the aluminum shield. It is observed that the ring structure is apparent for the aluminum projectile but not so apparent for the 3.6 mm nylon projectile shown in figure 4 (a) and (b). Moreover, there seems to be no dependence of the crater depth on the radial distance from the impact center for both the stressed and unstressed coupons and for the aluminum and nylon projectiles. The titanium coupons impacted with plumes from Aluminum projectile-Aluminum shield showed concentric ring structures that are reflective of the projectile diameter and the plume generated from the projectile impact with the aluminum surface. Although the ring structure exists, the lack of dependence of the crater depth on the radial distance from the center suggests that the craters were generated by aluminum particles released from the aluminum bumper and landed on the outskirts of the aforementioned rings of particle damage. As shown in Figs. 3 and 4, secondary impacts resulted in similar damage maps on the stressed and unstressed coupons for the Al and nylon projectiles respectively. The nylon density is almost three times less than the aluminum density with a lower melting and vaporization temperatures. With similar impact loading pressure on the aluminum, the nylon projectile vaporizes and the resulting plume is primarily made up of particles released from the aluminum shield. These particles are on the average greater in size than those released from impacts of aluminum projectiles on the aluminum shield.

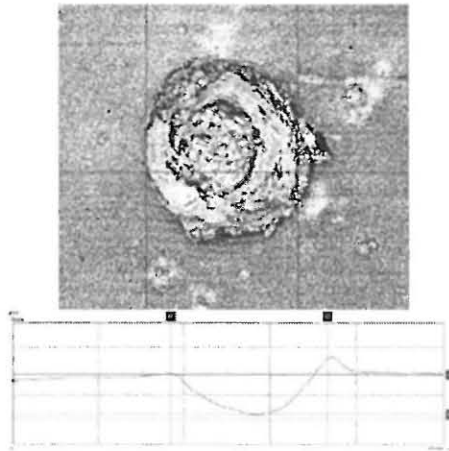


Fig. 2. Shows a 3D microscope image of a crater of 0.545 mm x 0.619 mm and 147.6 micron of depth equivalent to 12% depth of penetration.

Crater I.D.	Ti-6Al-4V Rear Wall Crater Damage	Penetration
HITF08373-5	0.545mm x 0.619mm x 147.6µm deep	11.6%
HITF08373-14	0.768mm x 0.676mm x 175.7µm deep	13.8%
HITF08373-19	0.537mm x 0.847mm x 203.8µm deep	16%
HITF08373-20	0.695mm x 0.684mm x 102.6µm deep	8.1%
HITF08373-21	0.716mm x 0.472mm x 164.5µm deep	12.95%

Table 2. Shows the depth of penetration for the 5 craters measured on the titanium coupon from a 1.6 mm aluminium projectile impact on aluminium.

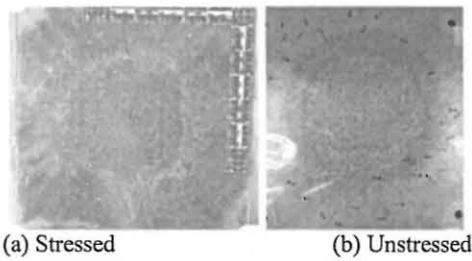


Figure 3 (a) and (b) shows the secondary plume impact on stressed and unstressed Titanium for a 2.6 mm aluminum projectile at 6.96 km/s and 7.32 km/s respectively

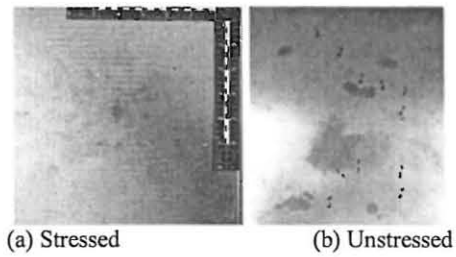


Figure 4 (a) and (b) shows the secondary plume impact on stressed and unstressed Titanium for a 3.6 mm Nylon projectile at 7 and 6.87 km/s

In the crater analyses performed at the NASA-Johnson Space Center, the crater depth and diameter were measured at selected damage sites. The average damage depth for each of the titanium coupons was calculated from the various craters. Figure 5 shows the crater depth plotted as a function of the projectile kinetic energy for the stressed and unstressed coupons with the 95% confidence interval calculated for the stressed coupons' measured craters shown in Fig. 5(b). The decreasing trend at higher projectile kinetic energy may be explained by the smaller particles in the plume generated by the higher loading impact pressure from the bigger aluminum projectiles.

### 3.2 Micromechanical-Metallographic Analyses.

The micromechanical analyses performed at WSTF focused on assessing the micromechanical properties of the titanium near selected craters of specific penetration depths. Three craters were chosen from three titanium coupons. Two craters came from the titanium coupons of tests HITF 08373 and HITF08375 respectively whereas the third from the titanium coupon of HITF08377. These three craters were chosen on the titanium coupons and a small sample was cut around each of the craters. The craters' depths were about 12%, 25% and 38% of the titanium thickness.

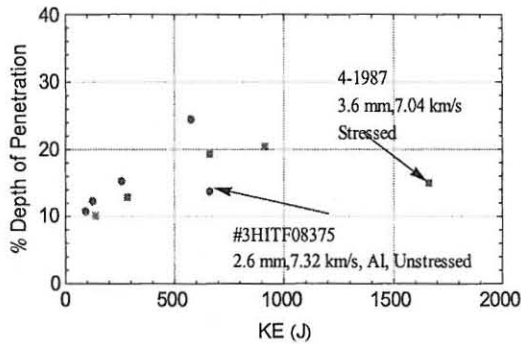


Figure 5 (a) shows the depth of penetration as a function of the projectile kinetic energy. Blue circles (red squares) correspond to the unstressed coupons (stressed coupons).

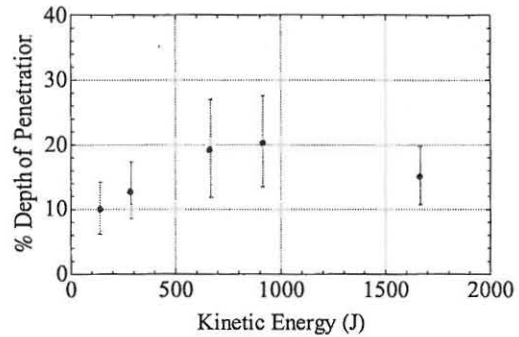


Figure 5 (b) shows the 95% confidence interval depth of penetration as a function of the projectile kinetic energy for the stressed Ti coupon.



### 3.2.1 Scanning Electron Microscopy

At first, scanning electron microscopy was performed on the three samples to obtain a crater profile and determine an accurate depth of the crater. Figs. 6 and 7 show SEM images of the craters from the 1.6 and 2.6 mm aluminum projectile whereas Fig. 8 shows an image of the crater that resulted from the nylon impact on the aluminum bumper.

### 3.2.2 Replica Metrology and White Light Profilometry

In an effort to assess the effectiveness of making a replica for the damage which in turn will be used for white light profilometry, replica metrology was performed on the craters utilizing a polymeric rubbery system. The replicas were allowed to cure and detached from the target plate on both the crater side as well as the back side in the region situated just below the crater. White light profilometry was performed on the single craters as well as on the plate surface just behind the crater prior to sectioning. As shown in Fig. 9, there is a close correspondence (a difference of 10%) between the replica and the crater obtained from the 1.6 mm aluminum projectile impact on the aluminum shield, and the results were consistent between the profiles acquired from the crater and the replicas.

### 3.2.3 Metallography

Once white light profilometry was completed, the craters were sectioned in the transverse orientation and the sectioned half crater was cold mounted and polished utilizing standard metallographic techniques. Once the mounted samples had been polished to approximately the middle of the crater, a Kroll's reagent was used to etch it. As shown in Figs. 10 and 11, the micrographs revealed equiaxed  $\alpha$  with intergranular  $\beta$  as would be expected for an annealed Ti-6Al-4V. Several spall cracks were observed (Fig. 11) on both sides of the sectioned crater for only the nylon impactor. The back side of the target plate just below the crater was also imaged and no spall cracks were observed. A direct comparison of the damage range for the nylon projectiles for both the stressed and unstressed Ti coupons shows that the maximum damage measured for the finite number of samples tends to be about 40%. Such deep depth of penetration presents concerns since it is shown later that the scanning electron micrographs of such deep impact exhibited spall microcracks near the crater.

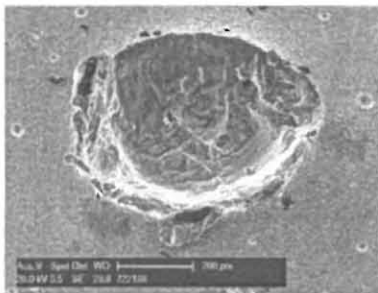


Figure 6. Shows an SEM of a crater from a particle in a plume resulting from 1.6 mm aluminum projectile. The crater's depth is 11.6% of thickness

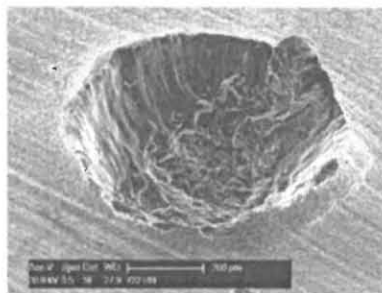


Figure 7. Shows an SEM of a crater from a particle in a plume resulting from 2.6 mm aluminum projectile. The crater's depth is 25.4% of thickness

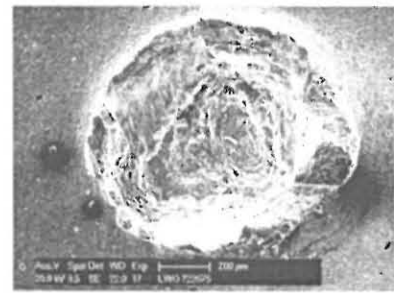


Figure 8. Shows an SEM of a crater from a particle in a plume resulting from 2.0 mm nylon projectile. The crater's depth is 38% of thickness

### 3.2.4 Vickers Hardness- Unstressed Titanium Coupons

Hardness was measured on the sectioned and mounted crater utilizing a Vickers microhardness tester with a 100 gram load. Hardness readings were taken on the base metal as well as from the base of the crater all the way to the back face of the target plate as shown in Fig. 12. The microhardness profile below the crater does not appear to show a very significant hardness change in the base metal as a result of the impact. For instance for the nylon projectile related crater, Vickers microhardness ranged from 285 HV to 326 HV whereas the base material hardness was found to be in the range of 300 to 350 HV with the highest reading located just below the front target plate face. Figure 13 shows a summary of the measured Vickers microhardness as a function of the distance below the crater for the three craters that were sectioned.

### 3.2.5 Energy Dispersive X-Ray Spectroscopy

Energy-dispersive x-ray spectroscopic (EDS) analysis was performed on control titanium samples as well as on the inside of the crater. The EDS technique is capable of detecting elements of atomic number 4 (Beryllium) and greater. As shown in Fig. 14 c, the inside of the crater possessed an intense aluminum peak which most likely is the result of deposition of the projectile (2017-T4 aluminum) or bumper plate material (6061-T6 aluminum) on the crater inner wall.

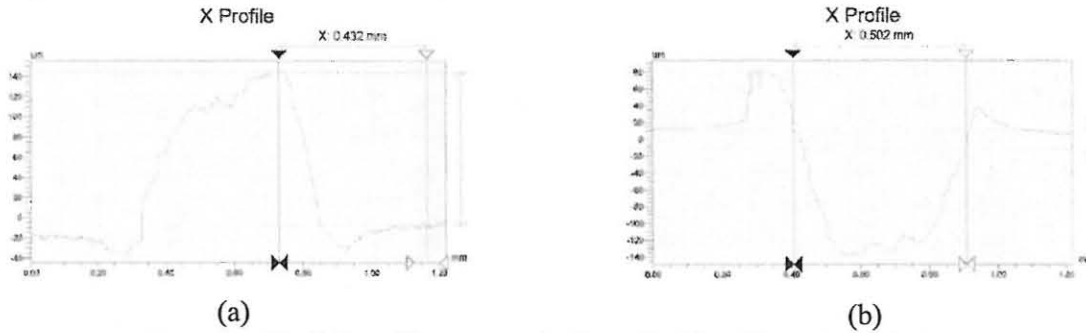


Figure 9. Shows the white light profilometry scan for the replica (a) and the crater (b) for the x profile.

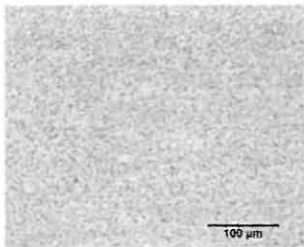


Figure 10. Equiaxed  $\alpha$  and intergranular  $\beta$  phases in the annealed Ti-6Al-4V alloy.

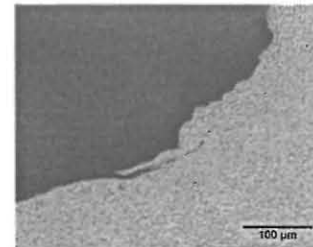
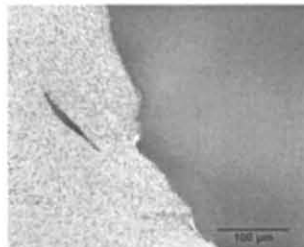


Figure 11. Shows two spall cracks on both sides of the sectioned crater for a nylon impactor.



### 3.3 Bumper Fragments Size Estimates.

An attempt was made to calculate the particle distribution for each of the impacts on the unstressed and shielded titanium coupons. Based on the ratio of the bumper thickness to the impacting projectile diameter  $t_b/d_p$  which ranged between 0.2 to 0.6, and on the projectile velocity being about 7 km/s, the projectile may have been partially or fully melted upon impact but the bumper unlike the projectile is fragmented and the fragments partially penetrated the titanium surface [Ref. 1.]. The craters produced from the aluminum projectile impacts and that were chosen for depth measurements lied on the outskirts of the ring structures that formed on the titanium. These craters were created by aluminum fragments that were broken off from the bumper. The nylon projectile most likely vaporizes upon impact and consequently, the craters are also formed from the aluminum fragments that are broken from the shield.

The crater depth information was used to approximate the diameter or the length scale of the impacting fragments. This was done using the penetration depth equation and back calculating the impacting diameter. The penetration depth that results from an impacting particle of diameter  $d_p$  and a velocity  $V_p$  is given for  $\rho_p/\rho_t < 1.5$  by [Ref.2.],

$$P_\infty = \frac{5.24 d_p^{19/18}}{\sqrt[4]{H}} \sqrt{\left(\frac{\rho_p}{\rho_t}\right) \left(\frac{V_p}{C}\right)^{2/3}} \quad (2)$$

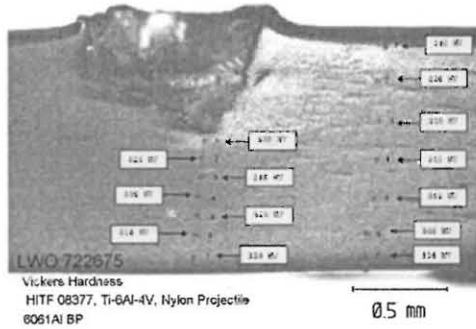


Figure 12. Shows the Vickers hardness measurements of the surface below the crater related to the nylon impactor on aluminium bumper.

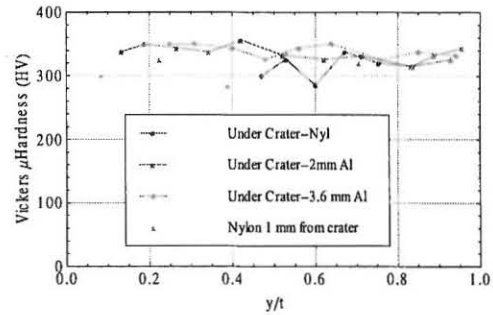


Figure 13. Summary of the Vickers hardness data plotted as a function of ratio  $y/t$  of the distance from the bottom of the crater ( $y$ ) to the titanium sheet thickness ( $t$ ).

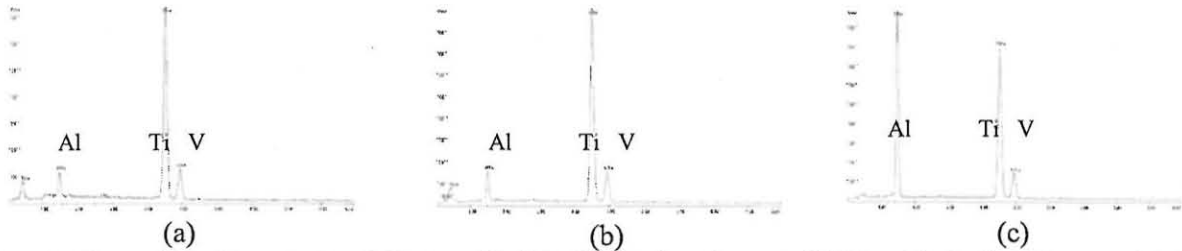


Figure 14. Shows the EDS spectra for a NIST traceable SRM (a), titanium plate material (b) and the inside of the crater (c). It is worth noting that the first peak in (c) is attributed to aluminum from the projectile or the bumper and that the NIST traceable SRM has extremely close signature to the titanium plate

$P_\infty$  is the depth in a semi-infinite target,  $H$  is the Brinell hardness,  $\rho_p$  and  $\rho_t$  are the projectile and

target densities respectively, and  $C$  is the speed of sound in the material interacting with the projectile. The maximum fragment diameter from the aluminum bumper cannot exceed the bumper thickness. The velocity of the bumper fragments is related to the impact velocity by [Ref.2],

$$V_{\text{fragments}} = 0.8V_p e^{-1/d_p} \quad (3)$$

Combination of Eqns. 2 and 3, realizing that  $d_p$  in Eqn. 2 is actually  $d_{\text{fragment}}$ , and solving for  $d_{\text{fragment}}$  leads to,

$$d_{\text{fragment}} = \left( \frac{P_{\infty} \sqrt[4]{H}}{5.24 \sqrt{(\rho_p / \rho_t)} (V_{\text{fragment}} / C)^{2/3}} \right)^{18/19} \quad (4)$$

The distribution of the fragment diameter/length scale based on the depth of the few craters from the unstressed (Figs 5 (a), 5 (c) and 5 (e)) and stressed (Figs. 5 (b), 5 (d), 5 (f)) coupons that were measured is shown in Fig. 15 (a) through (f). In Fig. 15 (e) and (f), the distribution of all particles from all the impacts performed on the unstressed and stressed coupons is shown respectively. The range of the particles length scale is comparable for the stressed and unstressed titanium and for the different projectile diameters. The fragmentation distribution depends on the bumper properties and the projectile energy. The titanium cratering was used to gage the plume distribution.

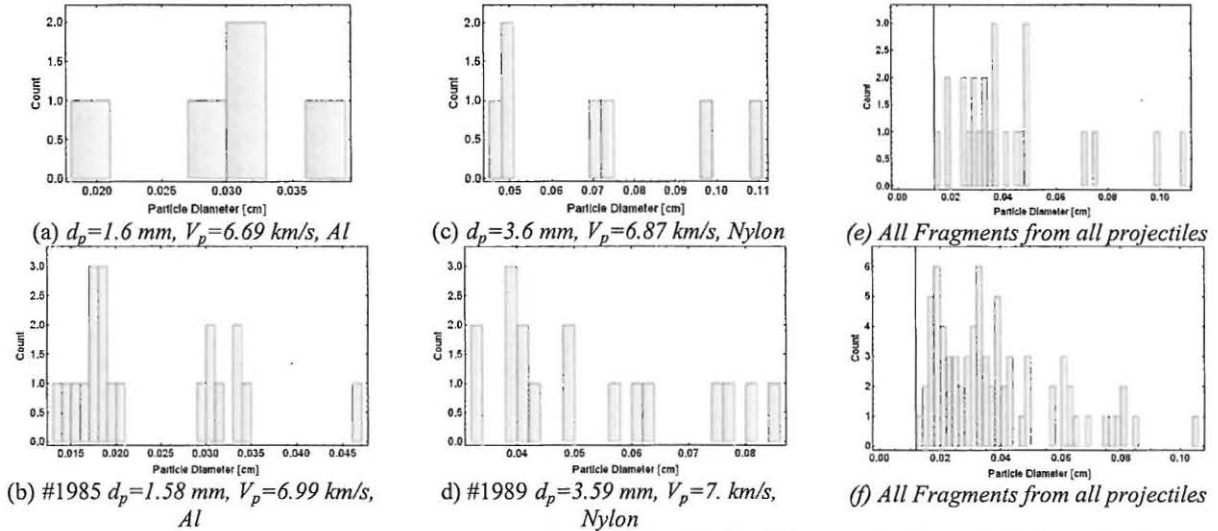


Fig. 15 Shows the fragmentation distribution from the crater data for the different projectiles used for impacting the unstressed and stressed titanium coupons that are shielded with an aluminum layer of ~ 0.04 inch in thickness

### 3.4 Residual Strength Measurements

The residual Strength measurements were performed at the NASA-Glenn Research Center. The tensile strength of the unstressed cratered titanium sheets was performed by using ASTM E8 [Ref. 3.] sub-sized specimens cut from the impact site. The 1" gage section of the test specimens was centered on regions exhibiting multiple, large craters or significant debris splatter. Prior to testing, the depth, width, and length of the largest craters in each gage section were measured. The largest craters were

~1.1 x 1.0 x 0.5 mm in width, length, and depth respectively. For the specimens exhibiting the worst apparent damage (i.e. largest craters), the strain field in the gage section was recorded during loading by using a camera-based displacement system. This allowed estimation of the local stress/strain concentration around the crater.

The engineering tensile properties of reference (undamaged) and cratered titanium sheets are given in Table 3. Very little difference in Young's modulus, yield strength, and ultimate strength are exhibited, however, significant differences occur for the fracture strength, elongation and area reduction. The lower fracture strength and ductility are a result of the MMOD causing localized yielding and premature failure as compared to a smooth section. The large ductility and fracture toughness of Ti-6-4 allowed load shedding and good ultimate strength. Although the tensile results indicate little change in some engineering tensile values, the local strain are substantially higher in some cases as shown in Fig. 16. The localized strains at net section yield are about 30% higher, and at failure they are more than 3 times higher. Thus it was concerning that the quasi-static tensile tests do not represent well the localized damage, and it might be expected that components subjected load-control failure scenarios, such as pressure vessels, could fail at lower section stresses over time, as load cannot be easily redistributed. To investigate this point further, a specimen with a 0.11x0.32x0.33 mm crater was held under a constant load of 110 ksi stress for 21 hours. The results showed a constant strain under this condition as depicted in Fig. 17. The concern is alleviated by the fact that the pressure is low compared to the usual high pressure common to pressure vessels and by Fig. 17 which shows no strain increase under constant load over a period of 21 hours.

Table 3. Shows the experimental results of the residual strength measurements.

The row labeled "Reference" corresponds to measurements of un-impacted titanium.

Plate Identification	Young's Modulus $E$ Msi	0.2% Yield Strength $S_{0.2}$ ksi	Ultimate Strength $S_u$ ksi	Fracture Stress $S_f$ ksi	Elongation $\epsilon_f$ %	Area Reduction $R_A$ %
Longitudinal Direction						
Reference	17.2	144	151	123	15%	34%
8606	17.5	144	153	148	11%	14%
8373	17.3	145	152	139	13%	24%
8374	17.5	145	153	136	14%	26%
8375	17.3	144	152	134	15%	29%
8376	17.3	144	152	149	11%	14%
8377	17.1	144	148	146	5%	8%

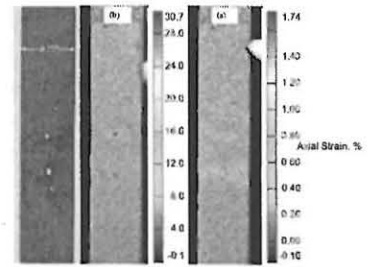


Fig. 16 Shows the localized strain field near a crater at yield and prior to specimen fracture. Note the extreme increase in strain at the crater location.

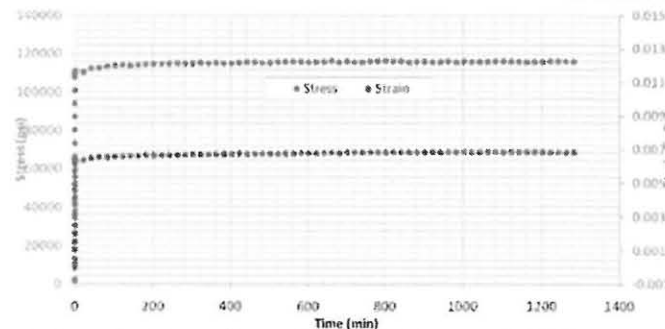


Fig. 17 Shows the stress and the strain of a specimen with one small crater of ~10% penetration of the TI thickness. The strain is shown to remain constant after 21 hours of constant loading at 110 ksi.

#### **4. Concluding Remarks**

In this paper, we showed the results of a series of hypervelocity impact tests in which a projectile is launched at an aluminum bumper in front of a titanium plate in order to understand the structure of the craters on the titanium caused by the projectile-bumper interaction and the resulting plume composed of projectile remains and target fragments. Several post impact tests performed on the titanium craters showed that the damage structures on the biaxially stressed and unstressed titanium plates were similar. Hardness measurements showed no differences between the Ti hardness under the crater and aside from the crater. This suggests that the local deformation upon impact does not affect the hardness properties even for the deepest crater of 28% depth analyzed in this work. Post impact residual strength measurements showed no discernable differences in the engineering strength properties between the pristine and cratered titanium. However, imaging of the strain field revealed significant increase in the localized strains upon tensile yield of the specimen. These measurements also revealed reduction in the fracture strength and reduction in ductility of the cratered titanium specimens. Tensile stress of 110 ksi applied to a cratered specimen showed no changes in the strain for a 21 hours duration which suggests that the constant load conditions at the operating stress of about 100 ksi is not as concerning as was thought.

We recommend performing burst pressure tests on cratered coupons. These tests are based on pressurizing the back surface of a cratered titanium coupon and increasing the pressure until failure. Such a test would be more representative of the load control failure than quasi-static tensile tests. We also recommend performing strain field measurements on craters of depth between 10 to 30% under loading conditions and comparing the strain fields, the elongation, area reduction and fracture strength for the two craters. This will help determine the appropriate allowable penetration depth on the surfaces of the metallic titanium pressure vessel.

#### **Acknowledgements**

The authors wish to thank the Orion program for funding these tests.

#### **References**

- [1] Cour-Palais BG. Meteoroid protection by multiwall structures, AIAA 69-372, 1969
- [2] Christiansen, E. "Meteoroids/Debris Shielding", TP 2003-210788, 2003
- [3] ASTM E8 / E8M - 08 Standard Test Methods for Tension Testing of Metallic Materials